PAPER

Check for updates

Utilization of biowaste-derived catalysts for biodiesel production: process optimization using response surface methodology and particle swarm optimization method†

Ikbal Bahar Laskar,[a] Tuhin Deshmukhya,[b] Aayushi Biswas,[c] Bappi Paul, [ID] [d]
Bishwajit Changmai,[c] Rajat Gupta,[e] Sushovan Chatterjee [ID] [f] and
Samuel Lalthazuala Rokhum [ID] *[c]

In this experimental and optimization study, banana (*Musa acuminata)* flower petal ash has been considered as an effective catalyst in the room temperature (28 °C) assisted transesterification to produce biodiesel from waste cooking oil. The transformation of *Musa acuminata* flower petals to ash catalyst has been performed by a simple conventional open-air burning process. Three important parameters (catalyst concentration, methanol/oil (M/O) molar ratio and time) that play a significant role in the conversion of waste cooking oil to waste cooking oil methyl ester (biodiesel) were investigated. In order to maximize the conversion rate these key transesterification parameters were optimized using central composite rotatable design of response surface methodology. A metaheuristic algorithm popularly known as particle swarm algorithm has been used to observe a clear picture of the global optimum points scattered around the search domain. Particle swarm optimization has also been used to validate the results obtained from central composite rotatable design. The chemical composition and morphology of the ash catalyst have been investigated using several analytical techniques. It was observed that the catalyst remained active until the 4th reaction cycle. The catalyst's reusability, renewability and robust activity in the reaction make it efficient, economic, green and industrially applicable.

1. Introduction

The rapid industrial growth coupled with uncontrolled population explosion has resulted in an overdependence on the fossil fuel, which is fast depleting and resulted in alarming global warming in recent years. Thus keeping in mind the current scenario, the need to discover environment friendly and renewable sources of fuel has been felt around the globe at present.[1,2] In the light of

[a] *Department of Mechanical Engineering, Jorhat Engineering College, Jorhat, Assam 785007, India*
[b] *Department of Mechanical Engineering, Barak Valley Engineering College, Nirala, Assam 788701, India*
[c] *Department of Chemistry, National Institute of Technology Silchar, Assam 788010, India. E-mail: rokhum@che.nits.ac.in; Fax: +91 3842-224797; Tel: +91 3842 242915*
[d] *Department of Chemistry, National Institute of Technology Nagaland, Dimapur, Nagaland 797103, India*
[e] *Department of Mechanical Engineering, National Institute of Technology Mizoram, Aizawl, Mizoram 796012, India*
[f] *Department of Mechanical Engineering, Cooch Behar Government Engineering College, Cooch Behar, West Bengal 736170, India*
† Electronic supplementary information (ESI) available. See DOI: **https://doi.org/10.1039/d2ya00011c**

this, biodiesel which is non-toxic, biodegradable and renewable has attracted widespread attention.[3] Though biodiesel production is expensive compared to fossil fuels, this factor can be nullified using low cost feedstock like non-edible[4] and waste oils.[5] Usually using vegetable oils the total cost of production becomes approximately twice the cost of fossil fuels wherein 60–75% of the cost involvement accounts for usage of vegetable oils.[6,7] Apart from this, the acute shortage of land for cultivation of edible vegetables is a big hindrance in commercializing edible vegetable oil-based biodiesel.[8] Thus, waste cooking oil (WCO)[9] which can serve as an alternative to vegetable oils in terms of availability and environment friendliness can be used as a cheap feedstock for low cost production of biodiesel.

Of late, the heterogeneous catalysts have gained attention due to their low cost of production compared to their homogeneous counterparts. Most importantly, the problems (expensive catalyst separation process, high wastewater generation during washing, saponification, non-reusable and additional reactant utilization) encountered with the homogeneous catalyst have made the researchers shift their focus to heterogeneous catalysts. Moreover, heterogeneous catalysts owing to their reusability and less corrosive nature have

become a favorable choice in biodiesel production.[10] The catalysts derived from rice husk,[11] banana peduncle,[12] banana peel,[13] *Brassica nigra* plant,[14] trunk of *Musa balbisiana Colla*,[15] *tucuma* peels[16] and *Citrus sinensis* peel[17] are some of the biomass waste-based solid catalysts that have been successfully used in the past few years. The outcome of some of these transesterification studies showed that the calcined ash samples of biomass can be used directly as heterogeneous solid catalysts without chemical modification. Balajii and Niju have managed to achieve a FAME yield of 98.69 wt% using Napoleon's plume seed oil and calcined banana peduncle ash.[12] In another study, Nath *et al.* obtained 98.87 wt% FAME yield using soybean oil and *Brassica nigra* plant ash.[14] Deka *et al.* considered yellow oleander seed oil and trunk of *Musa balbisiana* Colla for FAME production where a yield of 96 wt% has been recorded.[15] In order to counteract the high price linked with the use of vegetable oils as feedstock, various studies have been carried out to convert WCO into biodiesel using biomass based solid catalysts. These studies have reported the synthesis of various catalysts for conversion of WCO, such as oil palm ash,[18] lipase (enzyme),[19] egg shells,[20] chicken and fish bones,[21] chicken bones,[22] waste ostrich-egg shells,[23] eggshell and peat clay,[24] chicken manure[25] and white bivalve clam shell.[26] Tan *et al.* managed to obtain 89.5% biodiesel yield with chicken and fish bones as the catalyst from WCO at 65 °C.[21] In another study, Farooq *et al.* transformed WCO to biodiesel (89.33%) with chicken bone at a temperature of 65 °C for 4 h using 15:1 methanol to oil (M/O) molar ratio and 5 wt% catalyst loading.[24] Jung *et al.* used chicken manure as the catalyst to achieve a biodiesel yield of 95% from WCO with the expense of 350 °C.[25] Though these catalysts can successfully convert WCO to WCME, an elevated temperature of 60–100 °C is needed for completion of the reaction which demands high end facilities like condensers attached with a chiller, heater and temperature controller machine to name a few. This complex system which also demands tremendous amount of energy to run raises the biodiesel cost in return. In order to reduce the cost associated with temperature assisted biodiesel production approaches, Piker *et al.* managed to produce biodiesel from WCO at room temperature. Though a high biodiesel yield of 97% was achieved with 6:1 M/O molar ratio, it took 11 h for the reaction to complete.[6] In this current study, one of the major objectives is to reduce the conversion time of WCO to biodiesel using a biomass-based catalyst.

Banana the second largest produced fruit in the world[27] has a great potential in the yield of biodiesel. With a record global production of 101 992 743 MT in 2012, Africa alone accounted for a massive 15 863 068 MT.[13] Petals of banana flowers automatically peel out as the fruit grow and generate biowaste. Thus, disposal of peels and petals of banana waste have become a matter of concern for the countries where the production is high. Though catalysts derived from banana peel,[13] banana trunk[15] and banana peduncles[12] have already been studied in biodiesel production, the application of banana flower petals as a catalyst in transesterification reaction to produce biodiesel has not been reported in the literature.

The conventional catalysts with a micropore structure pose some inherent difficulties in converting large and viscous feedstocks (plant or algal oil) to biodiesel, whereas the mesoporous and macroporous catalysts have been seen to perform reasonably well.[28] Lee *et al.* carried out an extensive review on several solid acid and base catalysts' surface properties and pore architectures.[29] The study found that the catalyst carrying pore structures interlinked using meso- and macro-porous channels obtained an immense improvement in reaction rate due to the capability of diffusion of the reactants in the pores which increases the biodiesel production rate. They also reported that micropore structure possessing catalysts showed lower activity in the transesterification reaction due to the lack of active site accessibility in the pores.[29] Carrero *et al.* planted a secondary mesoporous structure on the microporous H-β-zeolite to improve the diffusion of reactants into the pores to enhance the esterification of microalgal oil.[30] Thus, the mass transfer limitation of the reactants could be enhanced by improving the diffusion properties using the presented catalyst.

Several critical factors are responsible for the production of biodiesel. The parameters such as M/O molar ratio, catalyst loading, reaction temperature, and reaction time are some of the key variables that directly influence the yield. Optimizing these parameters thus becomes crucial in improving the efficiency of the biodiesel production.[31] Response surface methodology (RSM) is a powerful tool frequently employed by researchers to design experiments and record the effects of the variables on the final response. RSM has so far been used in numerous studies related to biodiesel to optimize its production.[12,16,20,21] Betiku *et al.* produced biodiesel from neem oil where they optimized the production process using RSM and artificial neural networks (ANN) where a yield of 99.1% and 98.7% is obtained respectively by these two methods.[1] Balajii *et al.* used central composite design (CCD) of RSM to optimize the two-step biodiesel production process parameters where CCD was applied in transesterification and predicted a biodiesel yield of 99.36%. Under the condition determined by CCD, a biodiesel yield of 98.69% was quantified experimentally.[12] Several studies related to optimization of biodiesel production from banana peel,[13] eggshell,[20] and chicken and fish bones[21] have been investigated using CCD.

By considering the fact that a huge amount of waste is generated from banana flower petals along with banana peels due to the high consumption of this fruit worldwide, this study aims to convert waste (*Musa acuminata* flower petals (MAFP)) into a novel catalyst by the simple conventional burning method. Our continuous effort on transforming biowaste into a valuable product as low-cost, renewable and biodegradable catalysts in various organic transformations[32,33] as well as in transesterification reactions[34,35] has directed us towards the investigation of *Musa acuminata* flower petal ash (MAFPA) as the catalyst for converting WCO to WCME. In order to optimize the reaction parameters (*i.e.* catalyst loading, M/O ratio and reaction time) experimental runs were designed with central composite rotatable design (CCRD) of RSM. A powerful swarm-based metaheuristic optimization technique, particle swarm

optimization (PSO), has been used to perform proper global optimization of important variables in order to improve the biodiesel yield. As per the authors' knowledge, this is the first ever application of any swarm based algorithm in the area of biodiesel research. Application of swarm intelligence in this area can help scientists and researchers to gain an insight about the optimum design variables that help in improving the yield by properly digging out global optimum points in the domain.

2. Experimental

2.1 Materials

WCO, collected from two distinct hotels of Silchar, Assam, India, contains some food debris and moisture which were removed by filtration through filter paper followed by heating at 120 °C. The properties of treated WCO were determined by ASTM methods which are listed in Table 9. *Musa acuminata* flowers were fetched from the local market of Fakirtilla, Silchar, to collect unused large petals for further use. Bromothymol blue (pK_a = 7.2), phenolphthalein (pK_a = 9.8), indigo carmine (pK_a = 12.2), 2,4-dinitroaniline (pK_a = 15.0), 4-nitroaniline (pK_a = 18.4), methanol and acetone were purchased from Sigma Aldrich. The acid value of WCO and biodiesel was determined by a standard titration method using phenolphthalein indicator[36] where it is seen that the percentage of free fatty acids (FFA) is 0.98%. Since the acid content is less than 2% pre-esterification is not needed. $CDCl_3$ (D, 99.8%, cat. no. DLM-7-100S, which was used as a solvent in nuclear magnetic resonance (NMR) analysis) was purchased from CIL Inc., USA. Methyl hexanoate (analytical standard, >99.8%, cat. no. 21599, used as an analytical standard for gas chromatography–mass spectroscopy (GC–MS) analysis) was procured from Sigma-Aldrich.

2.2 Catalyst preparation and characterization

Large petals of *Musa acuminata* were separated from the fruits. The petals were then thoroughly washed with distilled water and sun-dried. Subsequently the dried petals were burnt in air and ground to fine powder. The physicochemical property of the prepared ash was then determined using the following analyses which include XRD, XRF, IR, XPS, TGA, TEM, SEM, EDX, CO_2-TPD and BET. X-Ray diffraction (XRD) study of waste banana flower petals (BFP) was carried out on a Bruker AXS D8-Advance powder X-ray diffractometer with the following parameter setting: Cu-Kα radiation (K-Alpha1 wavelength, λ = 1.54056 Å and K-Alpha2 wavelength, λ = 1.54439 Å), 35 mA current, 40 kV generator voltage, 2θ in the range 15°–90° at a scanning rate of 2° min^{-1}. The catalyst elemental analysis was performed on a Bruker S4 Explorer X-ray Fluorescence (XRF) spectrophotometer. FTIR analysis was performed to determine the functional group of the catalyst and IR spectra were obtained on a 3000 Hyperion FTIR spectrometer (Bruker, Germany) within the range from 400 to 4000 cm^{-1}. The catalyst surface element and binding energy of the corresponding elements were identified by XPS analysis in a Thermo Fischer Scientific bearing model no. ESCALAB Xi+ instrument. Thermal

stability analysis was carried out by thermogravimetric analysis (TGA) on the model STA 409 Metzsch Geratebau GMBH (Germany) under nitrogen flow at a pressure of 1.5 bar and flow rate of 2 L h^{-1}. The catalyst (MAFPA) mass transfer and phase transition were studied in the range between 10 °C and 1000 °C with constant nitrogen gas flow. Scanning electron microscopy coupled with EDS analysis (determination of elemental composition) of the catalyst was carried out on model no JEOL JSM-7600F. SEM images were captured on an FEI Quanta 200 F, using an X-ray source made up of tungsten filament doped with lanthanum hexaboride (LaB_6) and connected with an ETD as the secondary electron detector operated at high vacuum with an acceleration tension of 30 kV. Samples are analyzed by spreading them on a carbon tape. JEM2100 equipment was used to capture transmission electron microscopy images of the catalyst. Surface area and pore volume of the MPS were found out by Brunauer–Emmett–Teller (BET) study and the analysis result as N_2 adsorption–desorption isotherm was determined on a Micromeritics ASAP 2010 using He as the carrier gas. Prior to analysis the catalyst was made moisture and atmospheric vapour free by degassing at 180 °C for 12 h. Furthermore the basic strength was tested by the Hammett indicator method using the following indicators with different acidity functions (H_-): phenolphthalein (H_- = 9.8), indigo carmine (H_- = 12.2), 2,4-dinitroaniline (H_- = 15.0) and 4-nitroaniline (H_- = 18.4). Anhydrous ethanol was used in the reaction. In the experimental run, 50 mg of catalyst and 10 mL of anhydrous ethanol were taken in a 25 mL round bottom flask and shaken well. The reactants were then allowed to rest for 2 h to attain a state of equilibrium. The gradual change in reaction colour indicates the base strength of the catalyst. When the catalyst strength is higher than the weakest indicator, a change in solution colour is observed, while it remains unchanged when the catalyst strength is lower than the strongest indicator.

2.3 Pretreatment of waste cooking oil

Waste cooking oil was obtained from a hotel in Silchar, Assam, India. A filtered paper was used to make the oil free of crude impurities. The filtrate was then washed 3 times with hot water to eliminate the impurities and the mixture was allowed to settle, which was then separated using a separating funnel. The washed oil was then heated at 120 °C for 2 h to remove moisture from the oil. The oil obtained was treated with charcoal to remove any remaining colored impurities. The saponification value and acid value of the pretreated WCO were found to be 184.37 mg KOH g^{-1} and 1.95 mg KOH g^{-1}. The oil was further used for the transesterification reaction with methanol in the presence of the MAFPA catalyst.

2.4 Transesterification of WCO

As free fatty acid (FFA) was found to be <2%, it required only one step transesterification for the conversion of WCO to WCME.[23,37] In this study, the transesterification process was performed at room temperature (28 °C) in a round bottom (RB) flask placed on a magnetic stirrer. The desired amount of

Table 1 Variables and experimental conditions of transesterification for 3 factor five level CCD design of RSM

Variables	Symbol	Units	Level				
			$-\alpha$	-1	0	1	$+\alpha$
MAFPA concentration	A	% w/w	1.98	3	4.5	6	7.02
M/O ratio	B	mol mol^{-1}	3.98	5	6.5	8	9.02
Time	C	h	1.32	2	3	4	4.68

$\alpha = 1.68179$, variables converted from coded (C) to un coded (UC) and are as follows: $A = 10X + 40$, $B = 1.5X + 6.5$, and $C = X + 3$.

methanol, oil and MAFPA was taken in a RB and the reaction was carried out for a specific time span. All the experimental runs were performed sequentially according to the transesterification parameter (MAFPA concentration, M/O ratio and time) values provided by CCD of RSM. The parameters selected for designing the experimental run with CCD are shown in Table 1. Once the reaction time was completed the resultant mixture was subjected to vacuum distillation (heating) for a particular time period in order to remove the excess methanol followed by separation of the catalyst from the reaction mixture through centrifugation at 3000 rpm. Next, two layers were obtained which consist of the WCME (biodiesel) at the top layer and the prepared catalyst with glycerol at the bottom layer. The top layer containing WCME is collected and stored in an airtight container for further analysis. The oil conversion after each run is estimated using ^{1}H NMR which is carried out on a Bruker Avance II (400 MHz) spectrometer using CDCl$_3$ as a solvent and tetramethylsilane (TMS) as an internal reference. The percentage conversion of WCO to WCME was estimated using eqn (1) given by Knothe.[38]

$$\% \text{ WCME} = 100 \times \frac{2A_{\text{Me}}}{3A_{\text{CH}_2}} \quad (1)$$

where % WCME is the percentage conversion of triglycerides to methyl esters. The factors 2 and 3 were derived from the number of attached protons at the α-carbonyl methylene and methoxy carbons, respectively. A_{Me} = integration value of methoxy groups of methyl esters and A_{CH_2} = integration value of α-carbonyl methylene groups in fatty ester derivatives. The conversion percentage (FAME conversion) was estimated by taking the integrated areas obtained from the peaks of methoxy groups (A_{Me}) in the FAME and α-CH$_2$ protons present in the triglycerides of waste cooking oil. The constituent of final biodiesel obtained with optimized conditions was determined using an Agilent 7890-GC, Jeol AccuTOF GCV-MS.

2.5 Experimental design for maximum biodiesel yield

Here in this study central composite design (CCD) coupled with surface methodology (RSM) has been used for designing and modelling the experiments as well as optimizing WCME. The application of CCD in the optimization of biodiesel using MAFPA catalyst as well as the effect of key variables (M/O molar ratio, catalyst concentration and reaction time) on the yield has been discussed here. Twenty different experimental runs were conducted separately ($2^p + 2p + c$, where, p = number of factor and c = center point number). The 2^p design in the current case with center points needed fewer runs whereby giving identical details regarding curvature as shown by a 3^p design.[21] The current CCD model comprises $2^3 = 8$ factorial points, $2 \times 3 = 6$ axial and $b = 6$ center points. The axial point α in this study is selected to be 1.68. The independent variables along with their upper and lower limits can be seen from Table 1. Finally, the CCD matrix in Table 2 shows the whole design matrix including real and coded independent variables.

To correlate the biodiesel conversion as response to the transesterification process variables, a mathematical model is developed. The interaction of input variables with output

Table 2 Experimental and predicted value of WCME conversion using CCD

Run	Point type	MAFPA concentration		M/O molar ratio (mol/mol)		Time (h)		Biodiesel conversion (%)		
		UC	C	UC	C	UC	C	Experimental	Predicted	RSE %
1	Fact	3	-1	5	-1	4	1	54	54.75	1.39
2	Centre	4.5	0	6.5	0	3	0	85.74	86.27	0.62
3	Fact	6	1	5	-1	2	-1	46.88	47.94	2.26
4	Fact	6	1	8	1	2	-1	34	33.85	0.44
5	Axial	7.02	$+\alpha$	6.5	0	3	0	77.57	77.34	0.3
6	Fact	3	-1	8	1	4	1	60.29	59.83	0.76
7	Axial	4.5	0	6.5	0	1.32	$-\alpha$	19	18.02	5.16
8	Axial	4.5	0	6.5	0	3	0	85.78	86.27	0.57
9	Fact	6	1	5	-1	4	1	95.28	94.53	0.79
10	Fact	4.5	0	6.5	0	3	0	86.82	86.27	0.63
11	Fact	4.5	0	6.5	0	4.68	$+\alpha$	83.84	83.94	0.12
12	Axial	4.5	0	9.02	$+\alpha$	3	0	57.56	56.99	1
13	Centre	4.5	0	6.5	0	3	0	86.63	86.27	0.42
14	Fact	3	-1	5	-1	2	-1	31.29	31.18	0.35
15	Axial	4.5	0	3.98	$-\alpha$	3	0	64.84	64.57	0.42
16	Centre	4.5	0	6.5	0	3	0	87.53	86.27	1.44
17	Axial	1.98	$-\alpha$	6.5	0	3	0	39.58	38.96	1.57
18	Fact	4.5	0	6.5	0	3	0	85	86.27	1.5
19	Fact	3	-1	8	1	2	-1	26.64	27.99	5.06
20	Centre	6	1	8	1	4	1	88	88.71	0.8

Avg RSE 1.28%

(biodiesel conversion) is formulated in the following equation (eqn (2)):

$$Y = \beta_O + \sum_{i=1}^{n} \beta_i X_i + \sum_{i=1}^{n} \beta_{ii} X_i^2 + \sum_{i=1}^{n} \sum_{j=1}^{i-1} \beta_{ij} X_i X_j + \varepsilon_i \quad (2)$$

where Y = response (WCME conversion), X_i, X_j = independent variable, β_O = intercept, β_i = first model co-efficient, β_{ii} = i factor quadratic co-efficient, β_{ij} = linear coefficients of the model for the interaction between i and j factors, and ε = the experimental error ascribed to Y.

Analysis of variance (ANOVA) was examined in Design-Expert 11.0 software. Next P-test and F-test were performed on each coefficient to ensure the statistical significance of each term in the fitted equation. The considerable value for F (within the level of 95%) and p (< 0.05) was chosen for the model to be significant[39] on top of this, the operational parameters were tested with regression and graphical analysis to quantify their optimal values.

The regression coefficient of determination or relative standard error (RSE) between the experimental and predicted outcomes was to determine the model reliability.[40] The RSE is estimated by eqn (3). The average RSE lower than 10% was acceptable.[41]

$$\text{RSE\%} = \sum_{i=1}^{n} \frac{|Y_{\text{exp}} - Y_{\text{pre}}|}{Y_{\text{exp}}} \times \frac{100}{n} \quad (3)$$

where Y_{exp} = experimental value, Y_{pre} = value obtained from the model, and n = total number of results.

2.6 Maximizing the yield using particle swarm optimization (PSO)

Inspired by the social, especially the foraging nature of the birds in nature, a metaheuristic algorithm has been developed by Kennedy and Eberhart (Kennedy and Eberhart, 1995) in the year 1995. PSO works by initiating a swarm of hypothetical birds or particles in a three-dimensional space and assigning them certain velocities. In this 3D design space, the position of each particle is represented by time, catalyst concentration and M/O ratio. Every position represents a potential solution of the problem and these solutions are evaluated with respect to the objective function which is the yield in the present case. The beauty of this algorithm is its inherent ability to maintain a fine balance between intensification and diversification in order to explore the entire domain as well as exploit the promising regions in the later stages of the run. PSO functions by obeying the following update equations:

To initiate the search process, a swarm of hypothetical particles (that represent potential solutions of the problem) are generated and random velocities are assigned to the particles. The objective function values are evaluated with respect to the positions of the agents and their individual fitness values (p-best) and the fitness value of the best particle (g-best) is recorded.[42] Here it is worth mentioning that the initial positions of all the particles are their respective personal bests. Based on these two values the particles update or change their positions and velocities by obeying the following equations:

$$\nu_{i+1}^d = \nu_i^d + c_1 r_1 \left(\text{pbest}_i^d - x_i^d \right) + c_2 r_2 \left(\text{gbest}_i - x_i^d \right) \quad (4)$$

$$x_{i+1}^d = x_i^d + \nu_{i+1}^d \quad (5)$$

The velocity equation has three principal segments which equally contribute to the particles' movement through the problem space. The first term takes into account the influence of the particles' previous velocity on the new velocity. A linearly decreasing inertia factor 'w' has been linked with this term which efficiently maintains the balance between intensification and diversification. The second and third terms are cognitive and social components which scale the distance between the particle's best position as well as the group's best position and the current position.

The fact that makes PSO a superior algorithm is that the particles retain the memory of the locations in the domain. The algorithm runs in an iterative fashion by constantly improving the positions of the particles and finally converging at a near optimal point. After every iteration, the positions are updated and the particles are made to move toward the best particle of the swarm. Soon within a few iterations, the particles converge near a good optimum value in the vicinity of the global best position. Here a linearly decreasing inertia weight is employed which makes the algorithm scan the multi-dimensional domain in the initial iterations and gradually converge to a promising optimum value at the end of the run.[43] To ensure efficient functioning of the algorithm, the algorithm centric parameters should be judiciously selected. It is quite logical to believe that the more the number of agents the better will be the result. However, increasing the number of agents increases the computational effort without much improvement in the output. So, the number of particles in the swarm should neither be too less nor too large.

3 Results and Discussion

3.1 Catalyst characterization

To identify the specific composition of the banana flower petal ash (MAFPA) catalyst, XRF analysis was conducted, and the results are presented in Table 3.

The important components which are responsible for catalytic activity in MAFPA catalyst as found from the analysis are potassium oxide (60.23%), silicon dioxide (21.3%), magnesium oxide (4.78%), calcium oxide (3.17%), chloride (3.91%) and phosphorus pentoxide (3.65%). Some metal oxides in minimal amount are also traced from the analysis which are listed in Table 3. A close inspection of Table 3 reveals that a highly basic K_2O is the major component of the proposed mango peel ash that boosts its catalytic activity to a great extent. It is a well-known fact that the mixed metal oxide performs better in transesterification reaction as compared to single metal oxide as the catalyst.[44–46] This translates to the fact that since the current MAFPA catalyst is composed of mixed metal oxides, an enhanced catalytic performance in the reaction can be expected. Rabie *et al.* improved the transesterification reaction using a dolomite supported CaO and MgO (dolomite@CaO/MgO) catalyst.[45] Hence, the presence of

Table 3 Composition of banana flower petal ash (MAFPA)

S. no.	Compound formula	Weight (%)
1	K_2O	60.23
2	SiO_2	21.3
3	MgO	4.78
4	Cl	3.91
5	P_2O_5	3.65
6	CaO	3.17
7	Na_2O	1.11
8	SO_3	0.71
9	Fe_2O_3	0.19
10	TiO_2	0.18
11	ZnO	0.16
12	Al_2O_3	0.15
13	Rb_2O	0.13
14	SrO	0.12
15	CuO	0.1
16	MnO	0.07
17	Cr_2O_3	0.04

CaO and MgO in MAFPA further increases the efficiency of the present catalyst in the reaction.

The results of XRD analysis of MAFPA are shown in Fig. 1a. It is evident from the figures that the major components of MAFPA are metal oxides and carbonates where potassium oxide and potassium carbonate are found to be present in high abundance. These can be seen from the characteristic peaks at 2 theta values which include 23.56, 25.37, 26.81, 28.56, 32.17, 32.7, 38.49, 40.50, 48.5 and 57.91 (JCPDS reference file no. 26-1327 and 49-1093). $CaCO_3$ and CaO were detected at $2\theta = 30.3$, 32.31, 37.21, and 53.65 (JCPDS file no. 87-1863 and 48-1467). The SiO_2 present in MAFPA can be determined from the inhabitancy of peaks at $2\theta = 29.72$, 41.31 and 43.45 (JCPDS file no 81-0069). Apart from the above mentioned constituents, various other peaks obtained at 2 theta values of 20.21, 20.86, 42.95, 46.31 and 44.65 are due to SO_3, P_2O_5, MgO, Na_2O and C molecules respectively assured from JCPDS file no. 72-1664, 87-0952, 87-0652, 77-2148 and 80-0017. 34. We have earlier reported a similar XRD pattern for *Musa acuminata* peel ash.[47]

EDS analysis was performed to get an idea about various elements present in the MAFPA and the results are presented in Fig. 1b. The analysis revealed the presence of K (45.44%),

O (41.84%), Ca (2.4%), P (2.03%), Mg (3.05%), Si (1.95%), and C (1.9%). The results obtained from EDS analysis are in good agreement with XRF and XRD analyses. In a study by Madhuvilakku *et al.* the authors found that the catalytic (ZnO–TiO_2) activity of mixed metal oxide in transesterification is significantly higher than that of their single oxide counterparts.[46] Hence, it is anticipated that the presented catalyst would exhibit better performance in the reaction due to the presence of several metal oxides in it inherently.

Further, thermogravimetric analysis (TGA) was performed for MAFPA catalyst and the results are furnished in Fig. 2a. A steady fall of 1.89% in weight up to 110 °C (due to evaporation) can be read from the trend seen in the figure.[16] Again under the influence of N_2, the weight of MAFPA further drops by 9.83% in between 115–290 °C due to thermal decomposition of the catalyst,[47] while after 290 °C, the further drop in weight is due to the carbonaceous material of MAFPA undergoing oxidation and elimination of CO_2, CO, *etc.*[16,17,47]

To get information about the functional group attached to the MAFPA, FTIR analysis was performed. Fig. 2b depicts the presence of number of bands appearing at different wave numbers. The band appearing at 3210 cm^{-1} corresponds to O–H stretching and can be attributed to the H_2O bending vibration.[13,47,48] The bands at 1640, 1398, 1122 and 705 cm^{-1} are due to C–O stretching and bending vibrations which are the characteristic peaks of metal carbonates (CO_3), while the peak at 1398 cm^{-1} is due to K_2CO_3.[13,49] The metal oxide surfaces adsorb CO_2 from the environment which results in the formation of metal carbonates in MAFPA.[47] However the bands at 1051 and 621 cm^{-1} and the band at 2340 cm^{-1} are due to the stretching of Si–O–Si[13] and M–O–K bonds (M = Si, Mg, *etc.*) respectively, while the absorption band at 864 cm^{-1} is due to isolated vibration of SiO_4, in $CaMgSiO_4$. This may be due to interaction of Ca^{2+} and Mg^{2+} with SiO_4.[13]

Further, SEM and TEM images of MAFPA were captured with an aim to get a clear view of the catalyst's peripheral morphology. The number of aggregate surfaces with a mesoporous structure can be seen in Fig. 3a–c. MAFPA exhibited porous glossy/glassy and spongy particles (Fig. 3c and e). A similar morphological
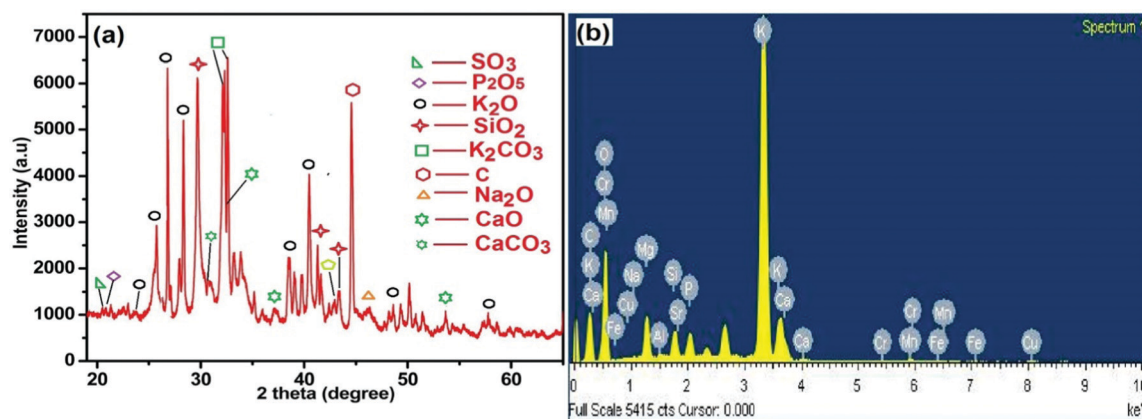
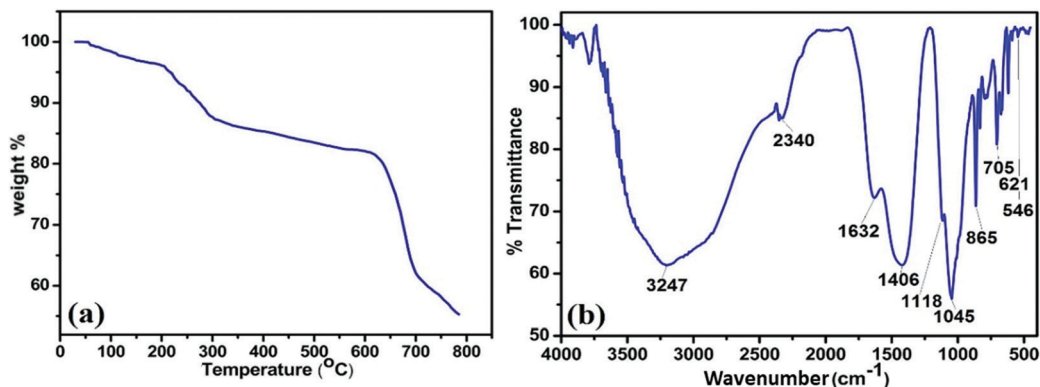**Fig. 1** (a) XRD pattern of MAFPA and (b) EDS spectra of MAFPA.

Fig. 2 (a) TGA pattern of MAFPA, and (b) FTIR spectra of MAFPA.

surface has been obtained from banana peel ash in our past studies.[47] A strong resemblance of results obtained by TEM analysis with that of SEM analysis has been noticed. From Fig. 3d, porous nature and assemblage of the particles can be seen. The crystalline nature of the particles was observed in the image obtained from SAED in Fig. 3f.

A type-IV hysteresis loop which is a characteristic of mesoporous materials is obtained in the N_2 adsorption – desorption isotherm of MAFPA (Fig. 4a). A clear insight about the pore size has been visualized from Fig. 4b where it is seen that the pores obtained are in the range of 4–35 nm. A similar mesoporous structure has been obtained in the SEM and TEM analysis.
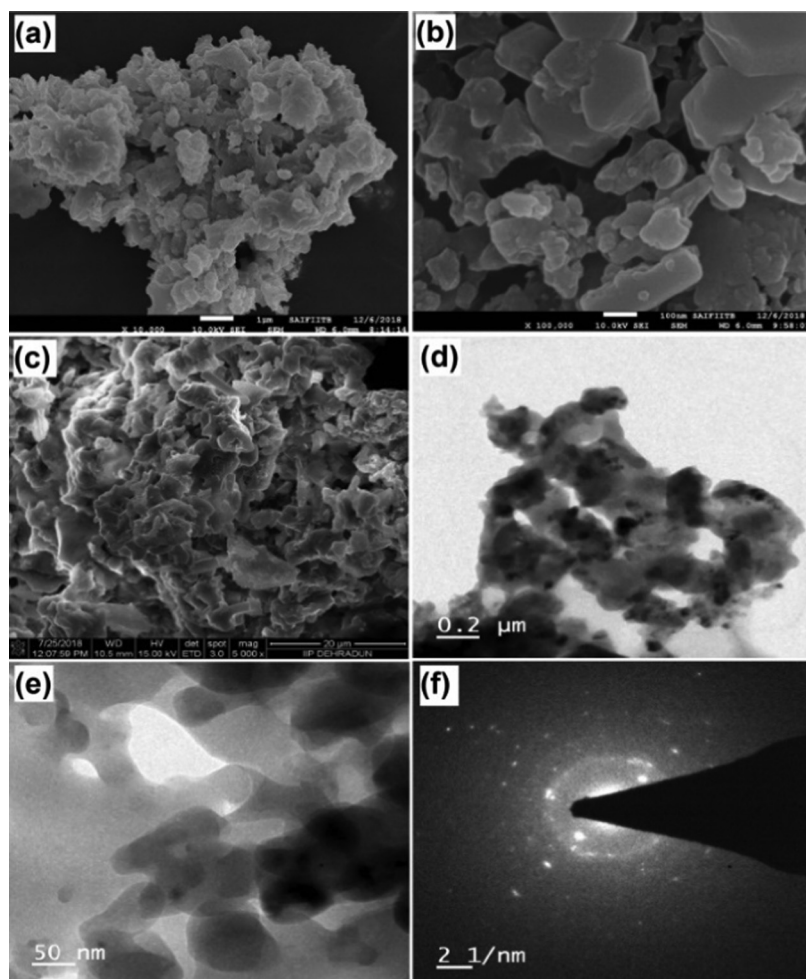
Fig. 3 SEM images (a–c), TEM images (d and e), and SAED pattern (f).

A surface area of 79.33 m^2 g^{-1}, pore volume of 0.260 cm^3 g^{-1} and pore size of 9.71 nm were determined by the BET method. The catalytic activity in transesterification reaction is greatly influenced by the surface area as well as the type of pore structure obtained.[29] The mesoporous structure helps in better diffusion of reactants inside the pores which eventually speeds up the reaction rate. This is in contrast to the microporous structures where reactions occur at the entrance, thereby reducing the rate of reaction.[28,29,50,51] The MAFPA being mesoporous in structure boosts biodiesel production to a large extent.

In order to have concrete information about the constituents present on the catalyst's surface, XPS analysis was performed. The results (as displayed in Fig. 5) showed that the most prominent constituents present in the MAFPA surface are potassium (23.5%), carbon (29.93%), oxygen (32.29 wt%), silicon (2.89 wt%), calcium (3.02 wt%), and chlorine (2.26 wt%). Along with these, magnesium (1.77 wt%), phosphorus (1.46% wt%), manganese (0.7 wt%), iron (0.15 wt%), strontium (0.77 wt%), aluminium (0.61 wt%) and copper (0.35 wt%) were also present in limited amounts. It can be seen from Fig. 5b that the C 1s signal is split into three parts along the binding energy through deconvolution. The peaks obtained can be attributed to the presence of adventitious carbon (283.53 eV), $C=O$ (284.53 eV) and CO_3^{2-} (288.33 eV).[52] However, in the O 1s core level spectrum (Fig. 5c), the presence of three different peaks at 529.63, 530.81 and 532.54 eV is due to the inhabitancy of metal oxide, alumina, and metal carbonates respectively in the MAFPA catalyst.[47]

Two peaks seen at 291.7 and 294.4 eV for K 2p indicated the presence of potassium bonded with carbonate and oxides (Fig. 5d).[53] The peaks obtained at 345.66 and 350.18 eV testify the presence of calcium carbonate and calcium oxide in the catalyst [Fig. S1a, ESI†]. From the Si 2p spectrum (Fig. S1b, ESI†), it can be stated that the peak at 104.4 eV is due to SiO_2, whereas the peak obtained at 101.36 eV can be attributed to silicate species.

Similarly, the Mg 1s spectrum shows two peaks at 1303.54 and 1301.46 eV respectively (Fig. S1c, ESI†). This can be credited to the bonding of Mg with O to form MgO and CO_3^{2-} to form $MgCO_3$ (Fig. S1c, ESI†). Sulfur (S 2p) was found

to be present in the catalyst in the form of sulfide and sulfate at 168.18 and 169.93 eV respectively (Fig. S1d, ESI†). The peaks at 131.73 and 133.99 eV in the P 2p spectrum were due to the presence of phosphate species (Fig. S1e, ESI†). Likewise, the peaks obtained at 197.7 and 199.7 eV respectively in the Cl 2p spectrum (Fig. S1f, ESI†) hint toward the presence of chloride species in the catalyst.

Determining the basic strength of the catalyst is important as the reaction rate in the base catalytic approach is highly influenced by its inherent basicity. The basic catalytic strength has been measured by the Hammett indicator method which was found to be in between $15 < H_- < 18.4$. This finding estimated that the banana flower petal ash catalyst is a strong base which can boost the transesterification at a faster rate. The high basic strength of the catalyst is mainly due to the presence of the metal-O group. Birla *et al.* found a similar basic strength value from a snail shell catalyst.[54] Pathak *et al.* observed the presence of various alkaline earth metals and alkali metals from *Musa acuminata* peel ash which is probably responsible for serving basic sites in transesterification reaction.[47] Here it is worth noting that the K in *Musa acuminata* peel ash is the major element. Thus K_2O acts as a strong base which is primarily responsible for high basic strength of the catalyst. Though the percentage of constituents varies marginally, a striking resemblance with respect to ingredients has been observed in between MAFPA and *Musa acuminata* peel ash. This similarity in characteristics can be a probable reason behind the high basic strength of MAFPA.

3.2 Optimisation of WCME conversion using RSM

The experimental value of WCME conversion was examined by CCD to obtain a regression model. The fit summary (Table 4) has suggested a quadratic model because of high values of R^2. This has fixed the quadratic equation as the best suited fit model for biodiesel conversion. A polynomial equation (eqn (4)) of second order was obtained through ANOVA analysis using Design Expert software to predict the WCME conversion.

$$\text{WCME conversion \%} = 86.27 + 11.41 \times A - 2.25 \times B + 19.61 \times C - 2.72 \times A \times B + 5.76 \times A \times C + 2.07 \times B \times C - 9.94 \times A^2 - 9.01 \times B^2 - 12.47 \times C^2 \quad (6)$$
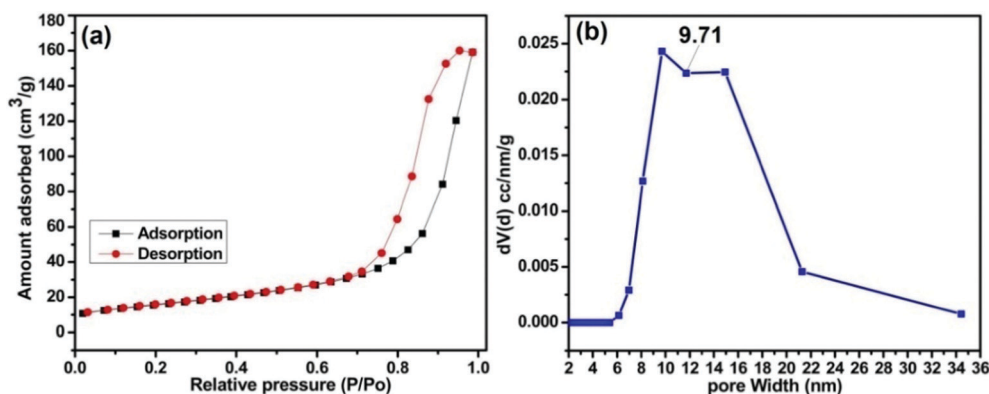

Fig. 4 BET result of MAFPA: (a) N_2 adsorption–desorption isotherm and (b) pore size distribution.
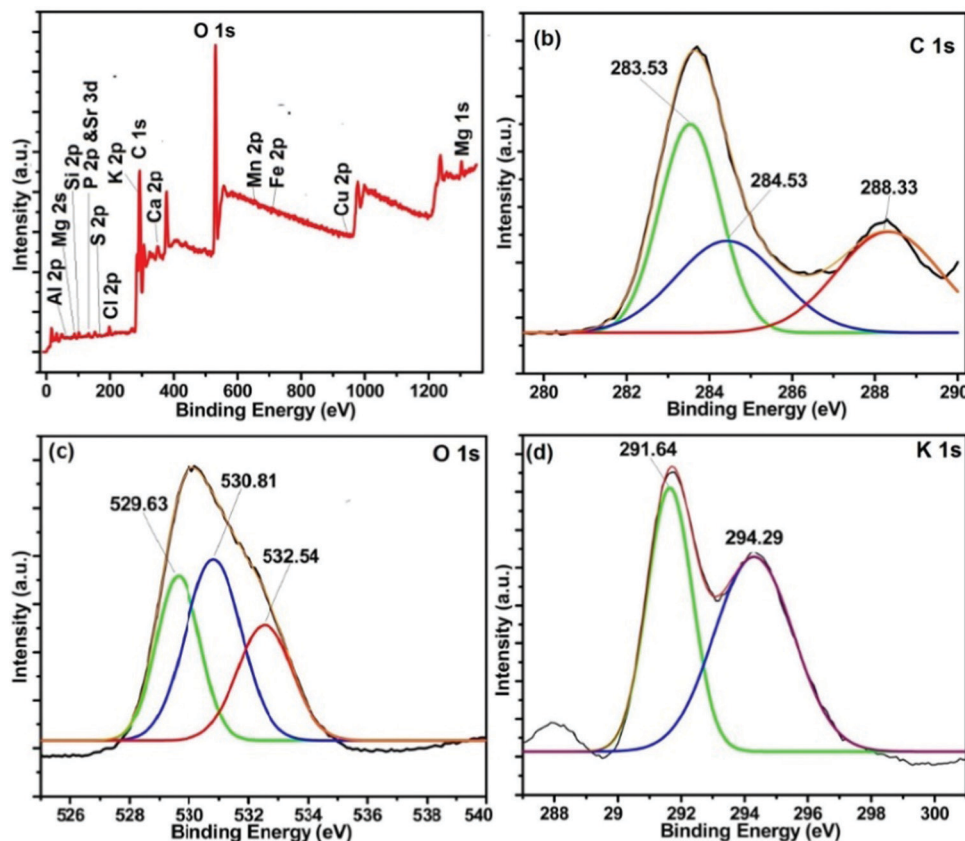
Fig. 5 XPS spectra of MAFPA: (a) survey, (b) C 1s, (c) O 1s and (d) K 1S core level spectra.

where transesterification parameters such as MAFPA concentration, M/O ratio and time are coded with A, B and C respectively. The interaction between the parameters is defined as AB, BC and CA, whereas A^2, B^2 and C^2 are their square terms.

From the ANOVA analysis shown in Table 5 it can be seen that the probability (p) value of the model is less than 0.0001 which signifies that the model is statistically significant and can accurately predict the experimental values. The R^2 value of 0.9991 too is a good indication of the model's ability to predict the experimental values with high accuracy. The significance of each factor was evaluated through P-value and Fisher's test (F-Test). The experimental data are significant with a confidence level of 95% because the model's F and p values are 1188 and <0.0001 respectively. The adjusted R^2 of 0.9982 implies that the variability between predicted and actual values is 99.82%. The R^2 value of 0.9991 signifies negligible deviation of predicted values from the actual ones. The lack of fit p-value as obtained from the lack of fit test is 0.31 which shows the lack of fit to be

insignificant. This testifies the fact that the experimental data have fitted successfully by considering interaction and contribution of all the factors in making regression response.[40,55]

Fig. 6a presents the actual *versus* predicted WCME conversion and it is clearly seen that the predicted values were very close to the actual values. The normal probability plot of residual is illustrated in Fig. 6b. It was seen that the errors were distributed normally around the straight line. Any value outside the interval ±5 is interpreted as a probable cause of operational error in the experimental data.[56] However, in the present case the standard residual values falling in between ±2 have been obtained as seen in Fig. 7.

3.3 Reaction parameter interactive effects on WCME conversion

The effect of the interaction of MAFPA concentration (A) and M/O molar ratio (B) on WCME conversion is presented on Fig. 8. The MAFPA concentration range was varied in between 1.98–7.02 wt%

Table 4 Fit summary of the CCD model for WCME

Source	Sequential P value	Lack of fit P value	R^2	Adjusted R^2	Predicted R^2	
Linear	0.0017	<0.001	0.6157	0.5437	0.4657	
2FI	0.6115	<0.0001	0.6468	0.4838	0.0798	
Quadratic	<0.0001	0.3405	0.9991	0.9982	0.9946	Suggested
Cubic	0.2131	0.6108	0.9995	0.9984	0.9654	Aliased

Table 5 ANOVA for WCME conversion

Source	Sum of squares	df	Mean square	F-Value	p-Value	
Model	11518.81	9	1279.87	1188.10	<0.0001	Significant
A-MAFPA concentration	1778.11	1	1778.11	1650.61	< 0.0001	
B-Methanol/oil ratio	69.30	1	69.30	64.33	< 0.0001	
C-Time	5251.64	1	5251.64	4875.07	< 0.0001	
AB	59.40	1	59.40	55.15	< 0.0001	
AC	264.96	1	264.96	245.96	< 0.0001	
BC	34.20	1	34.20	31.74	0.0002	
A^2	1424.53	1	1424.53	1322.39	< 0.0001	
B^2	1170.99	1	1170.99	1087.03	< 0.0001	
C^2	2241.66	1	2241.66	2080.92	< 0.0001	
Residual	10.77	10	1.08			
Lack of fit	6.62	5	1.32	1.60	0.3104	Not significant
Pure error	4.15	5	0.8302			
Cor total	11529.9	19				
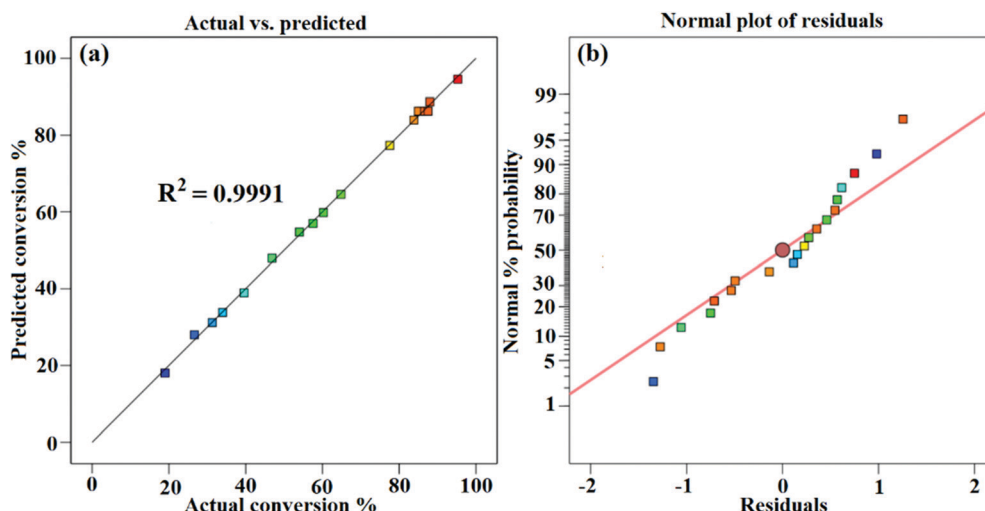
Fig. 6 Actual *vs.* predicted conversion (a) and normal plot of residual (b).

and the M/O molar ratio was varied in between 3.98 : 1–9.02 : 1, whereas the third parameter time was fixed to 3 h at the middle level. WCME conversion increased with the increase of parameter A and parameter B at the minimum level (3.98). However, after 6.63 wt% the WCME conversion started falling with the rise in parameter A. The reason behind this can be attributed to the unavailability of methanol to shift the reaction forward. Hence, surplus methanol is required to take forward the reaction towards completion. A similar observation has also been reported by Mendonça et al.[16] On the other hand, the WCME conversion is affected by increasing the parameter B while keeping A fixed at 1.98 wt%. When the parameter B increased beyond 6.86 : 1 M/O molar ratio, the conversion of WCME started dwindling. This trend of increase in conversion rate up to a certain limit is seen for all ranges of catalyst loading. A probable reason behind this is due to inhibition of the active catalyst surface by additional methanol. This results in lesser interaction or reaction of the catalyst with WCO.[57] The downfall in conversion can also be ascribed to the occurrence of reversible reaction. WCME reduction after a certain value has also been reported with *Musa acuminate* peduncle as a catalyst.[58] It can be noticed from the 3-D surface plot that the

maximum conversion of WCME was attained in a range of 5.58–6.3 wt% and in a range of 6 : 14–6.86 : 1. The significant inter-action among MAFPA concentration (A) and M/O molar ratio (B) is indicated by the lower P-value (<0.0001) of AB from Table 5.

The interaction of MAFPA concentration (A) and the reaction time (C) in the transesterification influenced WCME conversion which is shown in Fig. 9. The interaction of A and C has been elucidated by keeping the parameter B constant at 6 : 5 M/O ratio. The WCME conversion of <35% was seen from the graph for the parameters A and C at low level which is ascribed to less active surfaces present in the reaction and inadequate time for the complete transformation of WCO into WCME.[59] WCME conversion was increased sharply when the parameter A increased alone within a specific limit. This occurred because of the reactant's access to the high surface area (79.33 m^2 g^{-1}) of MAFPA catalyst resulting in high active sites to react and to move the reaction forward. A similar trend has also been obtained by other researchers in the past. Balajii et al. reported that the abrupt rise in biodiesel conversion with the rise in catalyst loading is due to the high surface area of *Musa acumi-nate* peduncle ash catalyst while converting *Ceiba pentandra* oil
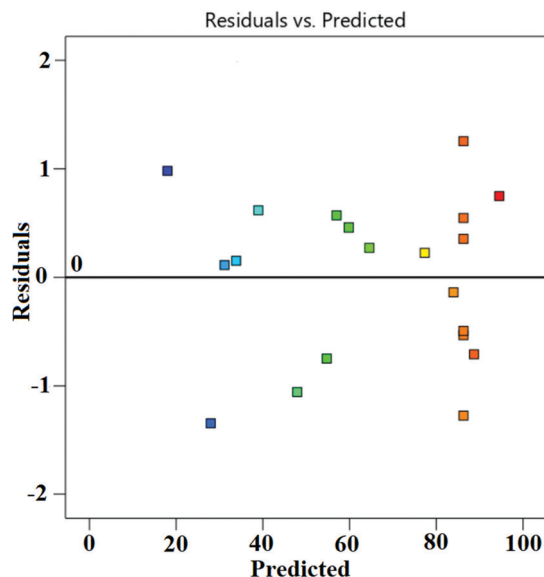
© 2022 The Author(s). Published by the Royal Society of Chemistry

Fig. 7   Residual *vs.* predicted.

Fig. 9   Interaction effects of time and MAFPA concentration.
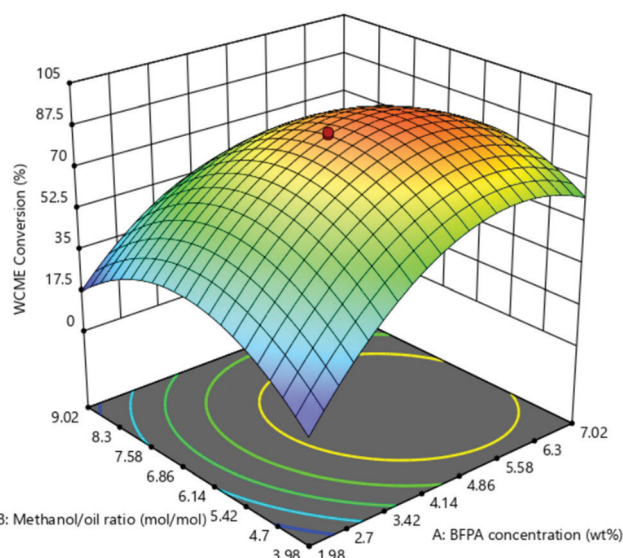

Fig. 8   Interaction effects of MAFPA concentration and M/O ratio.

to biodiesel.[58] Mendonça *et al.* noticed that the biodiesel conversion raised from 62.5% to 95.7% when catalyst loading is increased from 1 to 5 wt%.[16] But WCME conversion started to decline when the MAFPA concentration (*A*) loading exceeded 5.58 wt% and parameter *C* was at low level (2 h). This reduction in WCME conversion is due to the increase in the viscosity of the reaction mixture which leads to poor diffusion of reactants.[49,60] Betiku *et al.* noticed a similar observation and found that biodiesel yield gets reduced after 3.5 wt% catalyst loading.[13] Conversely, WCME conversion is greatly affected when time (*C*) is increased keeping *A* at low level. The conversion was seen to increase up to 3.91 h after which it decreased steadily. The increase in conversion is due to the availability of sufficient
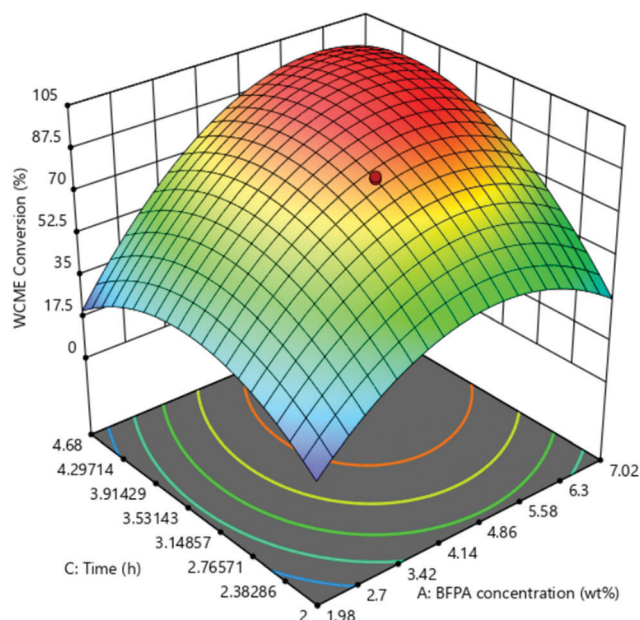
time for the active catalyst sites to react. However the fall after 3.91 h is due to the hydrolysis of esters which begins with a further increase in reaction time.[58] It was noticed from the 3-D plot (Fig. 10) that the maximum conversion was seen around 5.58–6.3 wt% for parameter *A* and 3.53–3.91 h for parameter *C*. The minimum *P*-value (< 0.0001) obtained by ANOVA (Table 5) is due to the effect of interaction between *A* and *C*. This obtained *P*-value testifies the statistical significance of the parameters.

The effect of parameters *B* and *C* on WCME conversion was simulated by keeping constant parameter C in the middle level as shown in Fig. 10. WCME conversion of $< 40\%$ was noticed at low values of both parameters *B* and *C* which indicated the need of extra methanol for the reaction to proceed further to completion. This fact is validated by the observed improvement in WCME conversion by increasing parameter B from 4 : 1 to 6.5 : 1. A similar observation has also been noticed by Balaji *et al.*[58]

With the rise in parameter *C* keeping *B* constant at low values the WCME comnversion increased immensly. This is due to the fact that the active sites of MAFPA got more time to come into contact with the reactants, resulting in more collisions which eventually enhanced the WCME conversion.[57] The parameter *B* after 6.86 : 1 M/O ratio with a time of 2 h deteriorated the WCME conversion. With high M/O ratio, reaction mixtures became dilute which decreased the contact between active surfaces of MAFPA and reactants.[16] Similarly at high M/O ratio and time, WCME conversion reduced due to glycerol's affinity to dissolve in the reaction mixture coupled with dilution of MAFPA concentration in surplus methanol.[58] From Fig. 10, the maximum conversion was noted in between 6.14 : 1–6.86 : 1 M/O ratio and 3.53–3.91 h. The statistical significance is registered since interaction of M/O ratio (*B*) and time (*C*) yielded a *p*-value of 0.0002 and high *F*-value of 46.59. All the plots displayed a drop in WCME conversion when all the parameters were kept at high level.
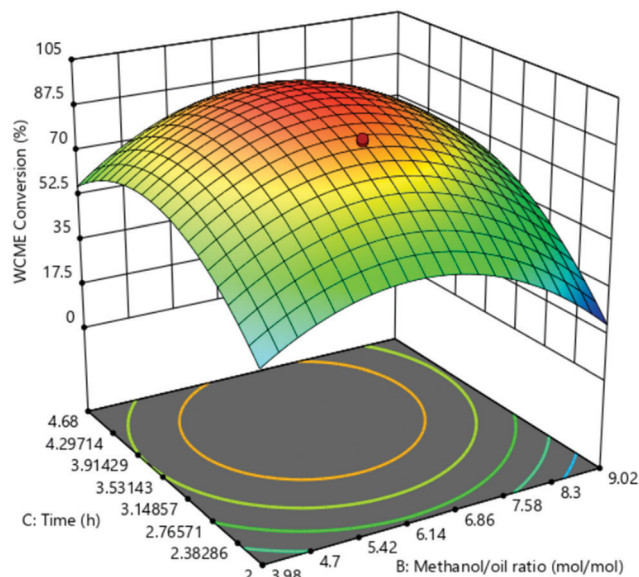
Fig. 10 Interaction effects of time and M/O ratio.

3.4 Optimization of transesterification parameters

3.4.1 Using design expert. In order to obtain the best parameter values accountable for high WCME conversion, the numerical method available in Design Expert software is applied and the proposed result is presented in Fig. 11. The regression model of the numerical method anticipated a highest conversion of 99.99% with an MAFPA concentration of 5.63 wt%, M/O molar ratio of 6.24 : 1 and time of 3.68 h. To validate the proposed result, proper global optimization of the parameters has been performed using PSO in the next section (Fig. 12).

3.4.2 Using PSO. The PSO algorithm used in the current study is coded by the authors in MATLAB 2015 and run in a computer having a 64-bit processor and 4 GB RAM. The code used a linearly decreasing inertia weight, which helps the algorithm to explore the search space in the initial iterations and exploited the promising regions in the later half of the search. Due to the stochastic nature of the algorithm, the code was run for 25 times and the best values have been reported. The parameters' values are reported in Table 6.
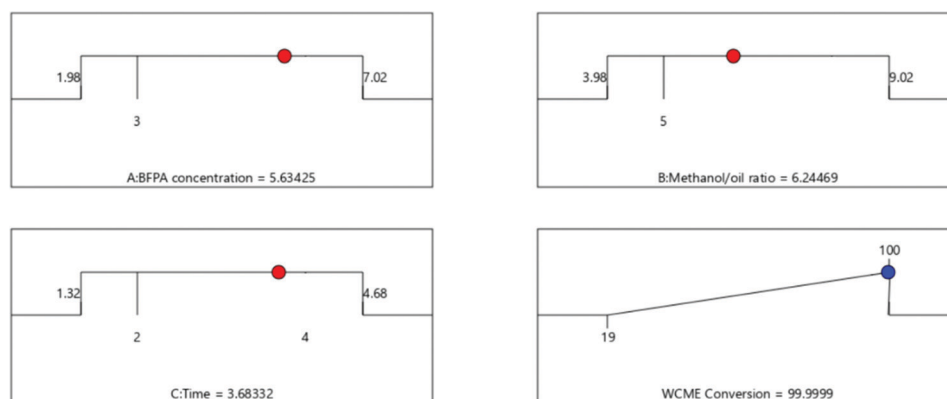
The swarm of 25 particles have converged around the 15th iteration. However, the algorithm was run for 100 iterations each time to make sure the particles do not fluctuate to newer points in the domain. From Table 7, it can be seen that the results obtained by PSO and CCD differ by a negligible amount of 0.08% which authenticates the findings. The transesterification of WCO is then performed experimentally under optimal conditions obtained from CCD using MAFPA catalyst and a conversion of 98.55 $\pm$ 0.4% (using eqn (1)) has been obtained.

3.5 Biodiesel charecterisation

3.5.1 ^{1}H NMR analysis. NMR spectrometry was selected to explicate the FAME formation from WCO and the result is displayed in Fig. 13. A singlet appearance has been observed at 3.66 ppm due to methoxy protons which confirmed the formation of biodiesel. Another important peak associated with confirmation of SOME formation was observed at 2.29 ppm for α-CH$_2$ protons.[49,58] A WCME conversion of 98.55 $\pm$ 0.5% was estimated using eqn (1) for the optimized operating conditions.

3.5.2 GCMS analysis. The constituents present in the prepared WCME were identified using GCMS analysis and the chromatograph of WCME is illustrated in Fig. 14. To determine each constituent in percentage, the predetermined area of the internal standard (methyl pentadecanoate, C15 : 0) was equated with the corresponding area of WCME. The identified components of WCME are listed in Table 8.

From the GC–MS analysis, it was observed that the principle components present in WCME are some unsaturated methyl esters such as methyl 11-octadecadienoate (52.3%) and methyl-11-ecosenoate (0.84%) as well as saturated methyl esters such as methyl hexadecanoate (34.31%), methyl tetradecanoate (5.36%) and methyl-nonadecanoate (2.22%), methyl -docosaanoate (1.97%), methyl tetracosanoate (1.81%), and methyl dodecanoate (1.16%). The physicochemical properties of WCO and WCME were evaluated and the results are compiled in Table 9.

3.6 Catalyst reusability

In order to ensure the efficiency of the catalyst in retaining the catalytic activity in successive cycles, reusability study has been performed.
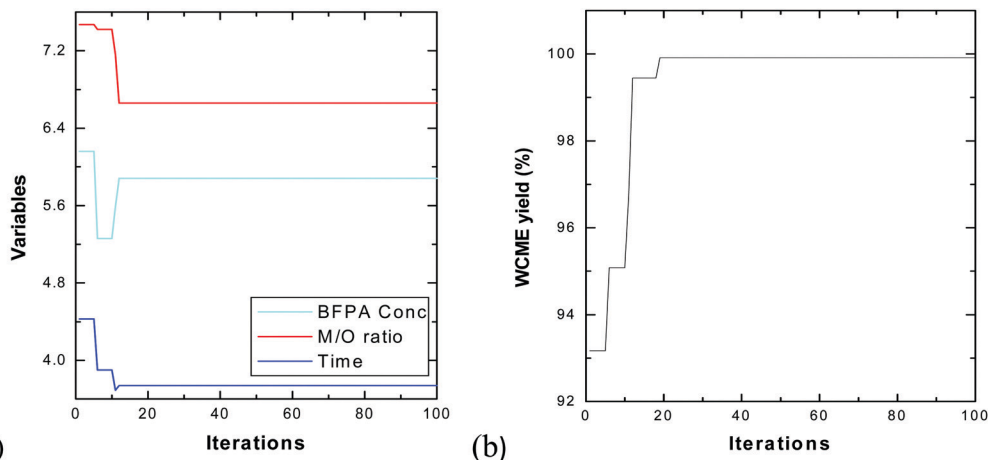

Fig. 11 Optimized operating conditions for WCME conversion.

Fig. 12 Convergence plots of (a) variables and (b) WCME yield obtained by PSO.

Table 6 Algorithm centric parameters of PSO[43] and their values

Algorithms	Parameters	Values
PSO	Number of birds	25
	Number of iterations	100
	c_1	1
	c_2	1
	w	Linearly decreasing from 0.9 to 0.4

Table 7 Validation of the results obtained by CCD with PSO

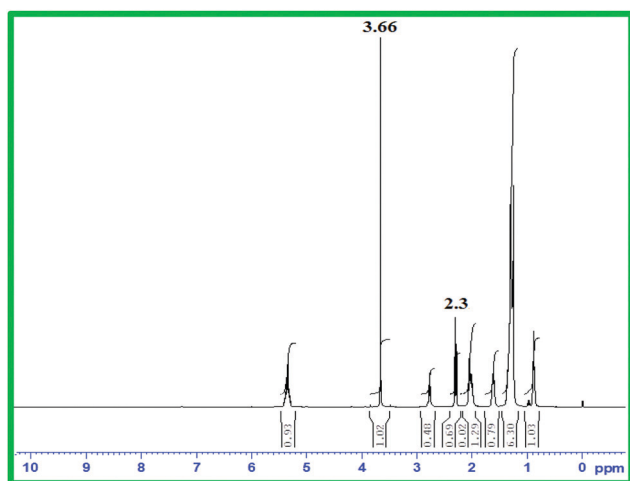| Methods	MAFPA (in %)	M/O	Time (in hours)	WCME yield (in %)
CCD	5.63	6.24 : 1	3.68	99.99
PSO	5.88	6.66 : 1	3.74	99.91

Fig. 13 ^{1}H NMR of soybean oil biodiesel.

After the completion of each cycle, the catalyst was reactivated for its application in the next cycle. Once the reaction

completed, the catalyst was collected through centrifugation and separated from undesirable materials by washing with distilled water and acetone followed by drying in an oven for 10 h at 100 °C. The recovered catalyst was tested for the subsequent reaction cycle under the optimal reaction conditions and the results are depicted in Fig. 15.

It has been deduced from the reusability study that a minimal fall in oil conversion to biodiesel yield occurs up to the 4th cycle. The oil conversion has abruptly dropped to 67% in the 5th cycle from 82% (4th cycle). This rapid downfall of catalytic activity in reaction was probably attributed to leaching of active sites of the presented catalyst. The EDS analysis of the spent catalyst (after the 5th cycle) clearly confirmed that the concentration of K significantly drops from 45.44 wt% to 21.82 wt% (see Fig. S2, ESI†) which is equivalent to 51.9% loss in potassium after the 5th cycle. The spent catalyst (after the 5th cycle) was also analyzed using XPS to identify the remaining elements in the catalyst after its repeated re-use in the reaction. The results of the analysis are listed in the ESI,† Table S1. The potassium percentage was found to fall from 23.5 wt% (fresh catalyst) to 13.79 wt% for the spent catalyst, which signifies a drop of 41 wt%. The full scan spectra and core level spectra of C 1s, O 1s, and K 2p are presented in the ESI† (Fig. S3). Hence, it is understood from XPS results that potassium ($K = 23.5\%$) occupies a large portion of the fresh catalyst. In the reused catalyst (after the 4th cycle), K concentration is quite high compared to other elements. Thus, K primarily in the form of K_2O and K_2CO_3 takes part in the transesterification reaction. Hence, the decrease in the K percentage in the catalyst affects the catalytic activity in the reaction to a large extent.

Moreover, the poor performance of the catalyst may also be due to the fact that the MAFPA surface absorbed oil, CO_2, moisture, impurities, glycerol and ester during its repeated use which resulted in agglomerated and larger particle size than the fresh MAFPA.[61] A larger particle size resulted in lesser exposed surface area, thereby reducing the active sites on MAFPA surfaces to interact with the reactant. This, along with leaching of active sites, is probably the reason for the significant drop in
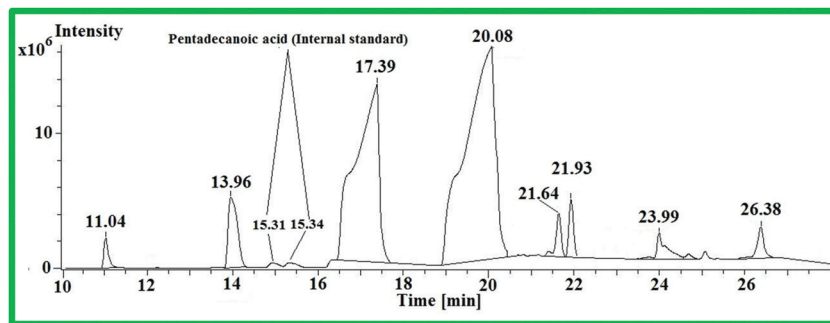
Fig. 14 GC spectra of WCME.

Table 8 Chemical composition of WCME

Peak No	R.t. (min)	Identified compound	Corresponding acids	Quantity (%)
1	11.04	Methyl dodecanoate	$C12:0$	1.16
2	13.96	Methyl tetradecanoate	$C14:0$	5.36
3	17.39	Methyl hexadecanoate	$C16:0$	34.31
4	20.08	Methyl 11-octadecanoate	$C18:1$	52.3
5	21.64	Methyl-11-ecosenoate	$C20:1$	0.84
6	21.93	Methyl-nonadecanoate	$C20:0$	2.22
7	23.99	Methyl-docosaanoate	$C22:0$	1.97
8	26.38	Methyl tetracosanoate	$C24:0$	1.81

Table 9 Physicochemical properties of WCO and WCME

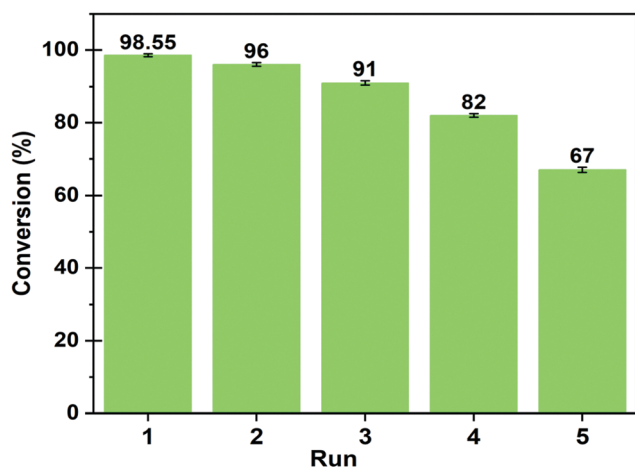| Properties	WCO	WCME	ASTM standard
Saponification value (mg KOH g^{-1})	184.37	—	D 5558
Acid value (mg KOH g^{-1})	1.95	0.52	D 664
FFA (%)	0.98	0.26	D 664
Kinematic viscosity (cst at 40 °C)	34.65	5.37	D 445
Density (g cm^{-3})	0.924	0.865	D 1448–1972
Cetane number	—	52	D 6890
Flash point (°C)	315	142	D 7215
Cloud point (°C)	−5	0	D 97
Pour point (°C)	−7	−2	D 2500
Copper strip corrosion	1 (a)	1 (a)	D 130

Fig. 15 Reusability of MAFPA catalyst at a catalyst concentration of 6 wt%, methanol/oil ratio of 6 : 1 and time of 4 h.

oil conversion in the 5th cycle.[29,62] This fact may be confirmed from the SEM, TEM and BET analysis of the reused catalyst (after the 5th cycle). SEM and TEM clearly exhibited agglomerated and larger size particles (Fig. S4, ESI†). A reduction in surface area has been seen from the BET analysis of the spent catalyst (after the 5th cycle). The BET surface area (53.335 m^2 g^{-1}) and pore volume (0.171 cm^3 g^{-1}) of the reused catalyst have remarkably decreased from the original value obtained for the fresh catalyst (Fig. S5, ESI†). In the fresh catalyst only a mesoporous structure was observed. However, in the pore size distribution of the reused catalyst, both micro and meso pores with an average diameter of 6.96 nm have been recorded. The occurrence of these micro pores in the reused catalyst may be due to partial blockage of pores.

4. Conclusion

In conclusion, a novel catalyst from waste banana flower petals was reported for the transesterification of WCO to biodiesel, WCME. The parameters of transesterification responsible for shaping WCO into WCME were optimized with CCD of RSM to maximize the conversion. The results were validated with a powerful global metaheuristic optimization technique, Particle Swarm Optimization (PSO), where all the important variables were simultaneously optimized to get a true picture of the fitness landscape. The regression model of the numerical method anticipated a highest conversion of 99.99% with an MAFPA concentration of 5.63 wt%, M/O molar ratio of 6.24 : 1 and time of 3.68 h. The presence of several oxides such as K_2O, SiO_2, CaO, MgO, MnO, CuO, SrO, *etc.* in the in the presented catalyst has resulted in high basic strength. The MAFPA catalyst can be reused up to the 4th cycle, affording a high 82% conversion of WCO to biodiesel. However, the catalyst activities reduced drastically on the 5th cycle, where a relatively low 67% biodiesel conversion was observed. The ash catalyst is extremely useful considering some crucial factors such as ease in synthesis, biodegradability, low cost, high reaction activity, biogenic and eco-friendly nature. These traits make the catalyst a ''green and sustainable catalyst'' for industrial scale biodiesel production.

Conflicts of interest

There are no conflicts to declare.

Acknowledgements

References

1 E. Betiku and S. O. Ajala, *Ind. Crops Prod.*, 2014, **53**, 314–322.

2 B. Changmai, C. Vanlalveni, A. P. Ingle, R. Bhagat and S. L. Rokhum, *RSC Adv.*, 2020, **10**, 41625.

3 S. J. Malode, K. K. Prabhu, R. J. Mascarenhas, N. P. Shetti and T. M. Aminabhavi, *Energy Convers. Manag.: X*, 2021, **10**, 100070.

4 M. A. H. Shaah, M. S. Hossain, F. A. S. Allafi, A. Alsaedi, N. Ismail, M. O. A. Kadirb and M. Idayu Ahmad, *RSC Adv.*, 2021, **11**, 25018.

5 Sahar, S. Sadaf, J. Iqbal, I. Ullah, H. N. Bhatti, S. Nouren, Habib-ur-Rehman, J. Nisar and M. Iqbal, *Sustain. Cities Soc.*, 2018, **41**, 220–226.

6 A. Piker, B. Tabah, N. Perkas and A. Gedanken, *Fuel*, 2016, **182**, 34–41.

7 S. Elias, A. M. Rabiu, B. Okeleye, V. Okudoh and O. Oyekola, *Appl. Sci.*, 2020, **10**, 3153.

8 S. Rezania, B. Oryani, J. Park, B. Hashemi, K. Kumar Yadav, E. E. Kwon, J. Hur and J. Cho, *Energy Convers. Manag.*, 2019, **201**, 112155.

9 P. Sharma, M. Usman, E.-S. Salama, M. Redina, N. Thakur and X. Li, *Waste Manage.*, 2021, **136**, 219–229.

10 G. Sahu, N. K. Gupta, A. Kotha, S. Saha, S. Datta, P. Chavan, N. Kumari and P. Dutta, *ChemBioEng Rev.*, 2018, **5**, 231–252.

11 C. Zhao, L. Yang, S. Xing, W. Luo, Z. Wang and P. Lv, *J. Clean. Prod.*, 2018, **199**, 772–780.

12 M. Balajii and S. Niju, *Renewable Energy*, 2020, **146**, 2255–2269.

13 N. Daimary, P. Boruah, K. S. H. Eldiehy, T. Pegu, P. Bardhan, U. Bora, M. Mandal and D. Deka, *Renewable Energy*, 2022, **187**, 450–462.

14 B. Nath, B. Das, P. Kalita and S. Basumatary, *J. Clean. Prod.*, 2019, **239**, 118112–118121.

15 M. Gohain, A. Devi and D. Deka, *Ind. Crops Prod.*, 2017, **109**, 8–18.

16 I. M. Mendonça, O. A. R. L. Paes, P. J. S. Maia, M. P. Souza, R. A. Almeida, C. C. Silva, S. Duvoisin and F. A. de Freitas, *Renewable Energy*, 2019, **130**, 103–110.

17 B. Changmai, S. Putla and L. Rokhum, *Ind. Crops Prod.*, 2020, **145**, 111911.

18 E. K. Sitepu, Y. Sembiring, M. Supeno, K. Tarigan, J. Ginting, J. A. Karo-karo and J. B. Tarigan, *S. Afr. J. Chem. Eng.*, 2022, **40**, 240–245.

19 M. Babaki, M. Yousefi, Z. Habibi and M. Mohammadi, *Renewable Energy*, 2017, **105**, 465–472.

20 T. S. Singh and T. N. Verma, *Energy Convers. Manage.*, 2019, **182**, 383–397.

21 Y. H. Tan, M. O. Abdullah, J. Kansedo, N. M. Mubarak, Y. S. Chan and C. Nolasco-Hipolito, *Renewable Energy*, 2019, **21**, 101317–101326.

22 F. Hussain, S. Alshahrani, M. M. Abbas, H. M. Khan, A. Jamil, H. Yaqoob, M. E. M. Soudagar, M. Imran, M. Ahmad and M. Munir, *Catalysts*, 2021, **11**, 630.

23 Y. H. Tan, M. O. Abdullah, J. Kansedo, A. Saptoro and C. N. Hipolito, *J. Appl. Sci. Process Eng.*, 2018, **5**, 277–285.

24 M. D. Putra, C. Irawan, Udiantoro, Y. Ristianingsih and I. F. Nata, *J. Clean. Prod.*, 2018, **195**, 1249–1258.

25 J. M. Jung, J. I. Oh, K. Baek, J. Lee and E. E. Kwon, *Energy Convers. Manage.*, 2018, **165**, 628–633.

26 S. Niju, K. M. Meera, S. Begum and N. Anantharaman, *Arab. J. Chem.*, 2016, **9**, 633–639.

27 D. Mohapatra, S. Mishra and N. Sutar, *J. Sci. Ind. Res.*, 2010, **69**, 323–329.

28 H. Wang, Y. Li, F. Yu, Q. Wang, B. Xing, D. Li and R. Li, *Chem. Eng. J.*, 2019, **364**, 111–122.

29 A. F. Lee and K. Wilson, *Catal. Today*, 2015, **242**, 3–18.

30 A. Carrero, G. Vicente, R. Rodríguez, M. Linares and G. L. Del Peso, *Catal. Today*, 2011, **167**, 148–153.

31 S. Dharma, H. H. Masjuki, H. C. Ong, A. H. Sebayang, A. S. Silitonga, F. Kusumo and T. M. I. Mahlia, *Energy Convers. Manage.*, 2016, **115**, 178–190.

32 K. Rajkumari, D. Das, G. Pathak and L. Rokhum, *New J. Chem.*, 2019, **43**, 2134–2140.

33 G. Pathak, K. Rajkumari and L. Rokhum, *Nanoscale Adv.*, 2019, **1**, 1013–1020.

34 B. Changmai, P. Sudarsanam and L. Rokhum, *Ind. Crops Prod.*, 2019, **145**, 111911–111921.

35 I. B. Laskar, K. Rajkumari, R. Gupta, S. Chatterjee, B. Paul and L. Rokhum, *RSC Adv.*, 2018, **8**, 20131–20142.

36 K. Rajkumari and L. Rokhum, *Biomass Convers. Biorefin.*, 2020, **10**, 839–848.

37 N. Mansir, S. H. Teo, U. Rashid, M. I. Saiman, Y. P. Tan, G. A. Alsultan and Y. H. Taufiq-Yap, *Renewable Sustainable Energy Rev.*, 2018, **82**, 3645–3655.

38 G. Knothe and J. A. Kenar, *Eur. J. Lipid Sci. Technol.*, 2004, **106**, 88–96.

39 K. V. Yatish, H. S. Lalithamba, R. Suresh, S. B. Arun and P. V. Kumar, *Process Saf. Environ. Prot.*, 2016, **102**, 667–672.

40 M. G. Nayak and A. P. Vyas, *Renewable Energy*, 2019, **138**, 18–28.

41 M. Barekati-Goudarzi, D. Boldor and D. B. Nde, *Bioresour. Technol.*, 2016, **201**, 97–104.

42 J. Kennedy and R. C. Eberhart, *Proc. ICNN'95 – Int. Conf. Neural Networks, Perth, WA, Aust. IEEE Xplore*, 1995, vol. 4, pp. 1942–1948.

43 T. Deshamukhya, D. Bhanja and S. Nath, *Proc. Inst. Mech. Eng. Part A J. Power Energy*, 2020, **234**, 1–14.

44 I. B. Laskar, L. Rokhum, R. Gupta and S. Chatterjee, *Environ. Prog. Sustainable Energy*, 2019, **39**, 1–11.

45 A. M. Rabie, M. Shaban, M. R. Abukhadra, R. Hosny, S. A. Ahmed and N. A. Negm, *J. Mol. Liq.*, 2019, **279**, 224–231.

46 R. Madhuvilakku and S. Piraman, *Bioresour. Technol.*, 2013, **150**, 55–59.

47 G. Pathak, D. Das, K. Rajkumari and L. Rokhum, *Green Chem.*, 2018, **20**, 2365–2373.

48 M. Sharma, A. A. Khan, S. K. Puri and D. K. Tuli, *Biomass Bioenergy*, 2012, **41**, 94–106.

49 I. B. Laskar, K. Rajkumari, R. Gupta, S. Chatterjee, B. Paul and L. Rokhum, *RSC Adv.*, 2018, **8**, 20131–20142.

50 I. B. Laskar, K. Rajkumari, R. Gupta and L. Rokhum, *Energy Fuels*, 2018, **32**, 12567–12576.

51 C. X. A. Da Silva, V. L. C. Gonalves and C. J. A. Mota, *Green Chem.*, 2009, **11**, 38–41.

52 L. M. Correia, R. M. A. Saboya, N. de Sousa Campelo, J. A. Cecilia, E. Rodrguez-Castelln, C. L. Cavalcante and R. S. Vieira, *Bioresour. Technol.*, 2014, **151**, 207–213.

53 B. Changmai, I. B. Laskar and L. Rokhum, *J. Taiwan Inst. Chem. Eng.*, 2019, **102**, 276–282.

54 A. Birla, B. Singh, S. N. Upadhyay and Y. C. Sharma, *Bioresour. Technol.*, 2012, **106**, 95–100.

55 H. Jaliliannosrati, N. A. S. Amin, A. Talebian-Kiakalaieh and I. Noshadi, *Bioresour. Technol.*, 2013, **136**, 565–573.

56 G. T. Ang, S. N. Ooi, K. T. Tan, K. T. Lee and A. R. Mohamed, *Energy Convers. Manage.*, 2015, **99**, 242–251.

57 M. A. Olutoye, S. C. Lee and B. H. Hameed, *Bioresour. Technol.*, 2011, **102**, 10777–10783.

58 M. Balajii and S. Niju, *Energy Convers. Manage.*, 2019, **189**, 118–131.

59 M. Gohain, A. Devi and D. Deka, *Ind. Crops Prod.*, 2017, **109**, 8–18.

60 S. H. Dhawane, T. Kumar and G. Halder, *Energy Convers. Manage.*, 2016, **122**, 310–320.

61 S. Sirisomboonchai, M. Abuduwayiti, G. Guan, C. Samart, S. Abliz, X. Hao, K. Kusakabe and A. Abudula, *Energy Convers. Manage.*, 2015, **95**, 242–247.

62 G. Joshi, D. S. Rawat, B. Y. Lamba, K. K. Bisht, P. Kumar, N. Kumar and S. Kumar, *Energy Convers. Manage.*, 2015, **96**, 258–267.